Aspect-ratio-constrained Rayleigh-Taylor Instability

J.T. Horne[a,*], A.G.W. Lawrie[a]

[a]*Hele-Shaw Laboratory, University of Bristol, Queen's Building, University Walk, Bristol, BS8 1TR, UK*

Abstract

In this paper, we study turbulent mixing between two miscible fluids that is induced gravitationally by Rayleigh-Taylor instability in a tightly confined domain. In our experimental configurations, one lateral dimension is between two and three orders of magnitude smaller than the other. Our motivation is to examine the relationship between domain width and certain key flow statistics, as the geometric restriction changes in relative significance. We match our experiments with carefully-resolved numerical simulations and in order to impose appropriate initial conditions, we extend Taylor's linear model of instability growth to characterise the influence of geometry on early modal development and use measured experimental data to inform our initialisation. We find that our experiments exhibit initial conditions with a k^{-1} spectral scaling of interfacial perturbation of volume fraction with a high degree of repeatability, where k denotes wavenumber. We discovered that our form of geometric restriction couples favourably with the spectral composition of our initial condition. We observe no early-stage transient relaxation towards self–similarity, because the instability already begins in that stable self–similar equilibrium, and this important special case has not previously been noticed despite decades of related research. We present our statistical observations from both experiment and numerical simulation as a validation resource for the community; such simulations are inexpensive to compute yet capture many dynamically significant properties.

Keywords:
Rayleigh-Taylor, experiment, geometric confinement, Hele-Shaw, Ekman friction, initial conditions, self-similarity, Direct Numerical Simulation

1. Introduction

1.1. History

The flow induced by relaxing the statically-unstable configuration of dense fluid overlying relatively less-dense fluid has been a phenomenon of considerable interest for over a century, beginning with a related experimental and theoretical contribution by Lord Rayleigh [1]. G.I. Taylor's work [2] considered the simplified case of two inviscid, incompressible and two-dimensional fluids in an unbounded domain, separated by a perfectly sharp, nominally horizontal interface, with small sinusoidal perturbations. If the amplitude were chosen to be much smaller than the wavelength of the instability, the equations of motion could be linearised and an analytical expression for modal growth obtained. Various extensions have been since been proposed to Taylor's model, in particular the viscous correction of Davies and Taylor [3] and the model of Duff et al. [4] accounting for non-ideal interface structure. More recent literature has focussed on the later-time behaviour where assumptions of linearity break down, beginning with Layzer [5]. Much later, Youngs [6] and Read [7] confirmed numerically and experimentally that for a broadband initialisation, non-linear growth of the mixed layer evolves quadratically with time.

Most historical work relates to unbounded Rayleigh-Taylor instability: the classical case. Only in isolated cases has attention been given to geometric confinement and the dynamical and morphological changes that this may introduce. Work by Lawrie and Dalziel [8] and Wykes et al. [9] considered vertical confinement by buoyancy, while Inogamov and Oparin [10] and Lawrie and Dalziel [11, 12] considered a tube-like geometry and exploited a separation of length- and time-scales to simplify the slow-time dynamics to one dimension, permitting analytical solution. While perfectly two-dimensional flows have been obtained controllably in the laboratory using soap film as the fluid medium, there is no known technique for producing variable-density flows, and especially those requiring unstable initial conditions. The closest analogue in the existing literature is based on a Hele-Shaw Cell [13], with Andrews and Spalding [14] performing an experiment in an almost-two-dimensional domain by overturning a thin tank containing a stable density stratification.

1.2. Mechanics of confinement

In the present work we take the same approach as Andrews and Spalding [14] and overturn a tank that can

*Contact details
Email address: jonathan.horne@bristol.ac.uk (J.T. Horne)

be enlarged in the thin direction by adding spacer elements. In its thinnest configuration, with respect to the viscous length-scale, the fluid is everywhere proximate to the boundary and is substantially influenced by it. Atmospheric flows are 'shallow' in the same sense as a Hele-Shaw cell, and are often treated as quasi-two-dimensional with contributions from boundary-friction modelled as an additional momentum-loss term in the dynamical equations. Geophysically, this term is known as *Ekman friction* [15], and we follow this convention here. Although the relationship between the magnitude of the Ekman friction and fluid depth is consistent across the literature,

$$\lambda \sim \frac{\nu}{b^2}, \tag{1}$$

where b is the fluid depth, ν is viscosity and $\frac{1}{\lambda}$ is a time–scale associated with the Ekman friction, there is substantial disagreement in the choice of scaling constant (e.g. Boffetta et al. [16] and Clercx et al. [17]) that appears to depend strongly on other specific details of these problems. We address this concern with regards to our configuration in §3 by returning to first principles and then validating our simulations against experiment.

While it is well known that there are morphological differences between two-dimensional, quasi-two-dimensional and fully three-dimensional flows, there are multiple factors that cause these differences. Ekman friction is only one such factor. Another, that is more deeply rooted in the mechanics of inertial flows, is the reversal of the scale-to-scale energy transfer. The Navier-Stokes momentum equation can be written in terms of vorticity transport $\frac{D\omega}{Dt}$ as,

$$\frac{D\boldsymbol{\omega}}{Dt} = \boldsymbol{\omega}.\nabla\boldsymbol{u} + \nu\nabla^2\boldsymbol{\omega} - \frac{\nabla\rho}{\rho^2} \times \nabla p, \tag{2}$$

where ρ is density, u is velocity, ω is vorticity, t is time and p is pressure. The baroclinic source term, $-\frac{\nabla\rho}{\rho^2} \times \nabla p$, and dissipative sink term, $\nu\nabla^2\boldsymbol{\omega}$, respectively add and remove vorticity from the system, but $\boldsymbol{\omega}.\nabla\boldsymbol{u}$ acts to redistribute vorticity between scales. A vortex filament with local vorticity $\boldsymbol{\omega}$ may be subject to a strain field $\nabla\boldsymbol{u}$, and when a principal strain axis aligns with $\boldsymbol{\omega}$ the filament must elongate. Conservation of circulation requires that the intensity of vorticity must then increase. However, the reverse process under negative strain (which on average will occur with equal likelihood as positive strain) can be shown to be unstable, and promotes breakdown of long vortical structures to smaller scales. As flows become geometrically constrained in one direction, velocity vectors tend to lie predominantly in the remaining plane, whereas the cross product $\boldsymbol{\omega} = \nabla \times \boldsymbol{u}$ increasingly points in the out-of-plane direction. Thus gradients $\nabla\boldsymbol{u}$ tend towards being orthogonal to $\boldsymbol{\omega}$, and the product $\boldsymbol{\omega}.\nabla\boldsymbol{u}$ tends towards zero [18].

In the special case of a field of homogeneous turbulence in an unbounded planar domain, the volume-averaged enstrophy, $\int_V \frac{1}{2}\boldsymbol{\omega}^2 dV$ evolves in time as,

$$\frac{d}{dt}\int_V \frac{1}{2}\boldsymbol{\omega}^2 dV = -\nu\int_V (\nabla\boldsymbol{\omega})^2\, dV, \tag{3}$$

and dimensionally the sink term scales as $\sim \frac{1}{L^4}$ per unit volume. The equivalent equation for volume-averaged energy,

$$\frac{d}{dt}\int_V \frac{1}{2}\boldsymbol{u}^2 dV = -\nu\int_V \boldsymbol{\omega}^2 dV, \tag{4}$$

scales as $\sim \frac{1}{L^2}$. Energy decay is therefore significantly weaker at small scales than enstrophy decay, yet both are direct functions of the same velocity field. In terms of energy density e on wavenumber shells κ,

$$\int_0^\infty e(\kappa)d\kappa = \frac{1}{2}\int_V \boldsymbol{u}^2 dV, \tag{5}$$

it follows that kinetic energy, $\int e(\kappa)d\kappa$, must decrease much more slowly than enstrophy, $\int \kappa^2 e(\kappa)d\kappa$, and the only consistent way to satisfy this requirement is for the function $e(\kappa)$ to increase over time for low κ and reduce for high κ. This transfer of energy in scale-space from high to low wavenumber occurs only when $\boldsymbol{\omega}.\nabla\boldsymbol{u} \to 0$. In the more general three-dimensional case, the vortex-stretching mechanism tends to dominate scale-to-scale transfer, but in the opposite direction: from low wavenumber to high.

1.3. Organisation

In this paper we investigate the Rayleigh-Taylor instability in the presence of geometric confinement. The configurations we examine address the statistical differences in behaviour as the classical unconfined case is progressively constrained towards two-dimensionality. We jointly use numerical simulation and analytical tools to match and interpret experimental measurement. Our focus here is the relationship between domain width and statistical quantities that characterise the flow, in the sensitive range where a small increase in width changes the morphological structure at observable length-scales. Certain statistics of interest are not available directly from experiment, but by careful validation we can obtain these by proxy from simulation. Firstly by extending Taylor's linear model to include Ekman friction, we develop a procedure for inferring initial experimental conditions in our thinnest configuration so that we can provide these for our simulations. Secondly, we measure the discrepancy in mid-plane scalar spectra between comparable simulations and experiments over the relaxation lifetime of the Rayleigh-Taylor instability, and use this measurement as a cost function on which to optimise the scaling constant of the Ekman friction for our problem. We also present experimental results from thicker domains and compare with simulation.

The paper is organised as follows: §2 discusses the experimental apparatus and its calibration, §3 outlines the analysis and procedure for obtaining suitable initial conditions in Ekman-dominated flow configurations, §4 summarises the numerical methods used in simulating these

flows, §5 proposes a theory on morphological features in an Ekman friction influenced flow and §6 presents our key findings on the effects of domain thickness, drawn from the comparison of simulation and experiment.

2. Experimental setup

In this section we describe the experimental apparatus, outline a method for calibrating for the lens distortion that is an unavoidable consequence of our configuration, and detail a colour calibration that is sufficiently sensitive to reveal manufacturing artefacts in the tank walls.

2.1. Apparatus

Our experiments used a thin tank with dimensions $1000 \times 250 \times b$ mm, where b is the thickness dimension varied between experiments. The tank walls consisted of two 10 mm transparent acrylic sheets with suitable grooves machined to house two sealing O-rings and a pattern of bolt-holes to distribute compressive sealing load around the tank perimeter. A metal distributor plate further spreads the load between bolt holes. The interior dimension for this slimmest configuration was $b \approx 1$ mm, approaching the limit of production tolerances on the materials used for this type of experiment. A sequence of acrylic spacer plates can be added to bring the total interior dimension up to $b \approx 12$ mm.

The canonical Rayleigh-Taylor configuration is not realisable in the laboratory, so we rely on careful quantification and good physical understanding to interpret measurements from non-ideal experiments. Particular emphasis is placed on the approach to initialise statically unstable density stratifications, because subsequent development has been shown to be highly sensitive to the spectral characteristics of the initial interface ([19]). Previous experiments have utilised one of three methods: acceleration of an initially stable stratification vertically downwards [7]; removal of a barrier at the interface of an unstable stratification [20], [21]; overturning of a stable stratification [14]. Experiments focussing on the morphology of the flow require long evolution time-scales relative to their vertical size, and it is advantageous to use small density differences between upper, u, and lower, l, layers. It is impractical to use the small Atwood numbers we desire,

$$A_t = \frac{\rho_u - \rho_l}{\rho_u + \rho_l} \ll 1, \tag{6}$$

with artificially accelerated reference frames, and barrier removal introduces undesirable vorticity at low wavenumber that would be particularly potent in planar geometries that restrict the breakdown of vortices by the vortex-stretching mechanism discussed in §1.2. Overturning the tank is a pragmatic approach for thin geometries, though it is well known that inertial forces during overturning cause the interface to rotate [22], and for a tall tank in the absence of dissipative contributions, the interface will have rotated away from the horizontal by $\theta = +\tan^{-1} 2\pi \approx 81°$. In practice, boundary friction and viscosity suppress the rotation, so while this behaviour was noticeable in the thickest of our configurations, $b = 12$ mm, the statistical quantities we seek were not unacceptably contaminated.

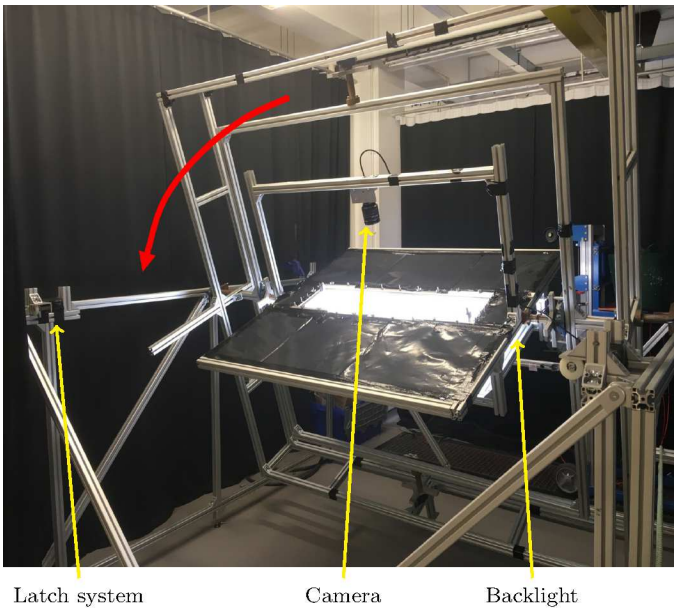

Figure 1: Experimental apparatus - a Hele-Shaw Cell mounted onto a rotating frame.

Our apparatus mounts the tank, backlight and camera on a large rectangular frame, as shown in figure 1. Weights attached to rope are released to initiate the rotation and an elastic bungee cord decelerates the frame before it engages with latches that prevent rebound. There needs to be sufficient residual angular inertia after deceleration to overcome the resistance of the latch, so some impulsive acceleration is unavoidably transmitted to the flow. While this may temporarily induce Richtmyer-Meshkov instability, the longer time-scale relaxation is very clearly dominated by Rayleigh-Taylor instability.

The experiments were configured such that the dense salt-solution layer was dyed with KTC Red Food Colour powder and the less dense layer left without dye. Calibration of the dye is described in §2.3. The densities were measured with an Anton Paar DMA 4500M density meter. In a typical experiment our Atwood number was $A_t = 9.7 \times 10^{-3}$, where the Boussinesq appoximation is valid. Video sequences were obtained using a Teledyne DALSA Genie TS-C2500 colour CMOS Bayer camera transferring data over a gigabit Ethernet link to a SSD hard-drive using in-house capture software to control the acquisition. A pair of 50 W LED light panels provided back-lighting behind a 3 mm opal semi-opaque acrylic sheet, providing uniform diffuse back-illumination. The LED panels were powered from a DC power supply to eliminate 50 Hz mains flicker.

The constraints of a moving reference frame for the

backlight, tank and camera limited the available distance between the tank and the camera to 0.5 m, and to capture a full field of view, we mounted an 8 mm Samyang fisheye lens on the camera. This introduced considerable spatial distortion, the handling of which is the subject of the next section.

2.2. Spatial calibration

An accurate mapping of image intensity I from camera pixel space to scalar concentration c in the moving reference frame is essential for our detailed comparison of simulation and experiment. A 25×91 calibration grid of regularly-spaced white dots on a black background was used to measure the relatively severe distortion induced by the fisheye lens and to define the geometric component of the mapping $I(\chi, \zeta) \to c(x, z)$. Unfortunately the distortion causes very large spatial variation in the projected light intensity falling on the camera sensor, so reliably identifying the dots was challenge in itself, since simple thresholding of intensity would fail to isolate them. Instead, a procedure based on a Markov process in graphs was used to binarise the image. There are many such approaches; we chose to classify light and dark by associating a local stochastic transition probability $\boldsymbol{T}_{ij}$ with local intensity gradient between the i'th pixel and an neighbouring j'th pixel, then defining a set $\boldsymbol{p}$ of initial probabilities of particles being located in various positions around the image (though always starting in the background). By repeatedly updating the probability vector according to the linear system,

$$\boldsymbol{p}_k = \boldsymbol{T}^k \boldsymbol{p}_0, \tag{7}$$

for some large k, we obtain the equilibrium probability distribution of particle location; a discrete analogue of the steady-state solution to the diffusion equation. For suitably chosen transition probabilities T, the likelihood of a particle crossing from dark to light is very small, so binary classification is then straightforward. Individual dots were then identified as isolated clusters of pixels using the well-known DBSCAN algorithm ([23]). Once a few adjacent dots had been identified, a local Taylor's expansion predicted the location of the next search region for a new cluster, greatly reducing the computational cost.

A reliable mapping will remain smooth in the presence of image noise and any uncertainties in dot position, have continuity in several derivatives and handle curvature in both x and y directions in the physical coordinate space. We developed a multi-variate extension of Legendre polynomials to use as an orthogonal basis on which to obtain a best-fit projection of the distances between dots. We satisfy the inner product in two-dimensions,

$$\langle p, q \rangle = \int_{-1}^{1} \int_{-1}^{1} p(x, y) q(x, y) dx dy = 0, \tag{8}$$

for suitable orthogonal basis functions p and q, evaluating polynomials of the form $a + bx + cy + dxy + \ldots$ up to fourth order and applying a Gram-Schmidt adjustment order by order to ensure mutual orthogonality in the function space. The optimal coefficients β_i for each of the 15 Legendre basis functions were calculated by forming an over-determined linear system,

$$\boldsymbol{L}\boldsymbol{\beta} = \boldsymbol{\chi'} \tag{9}$$

where each column of a matrix $\boldsymbol{L}$ is generated by a single basis function, and each row represents a chosen point in space. The right-hand-side vector $\boldsymbol{\chi'}$ represents discrete evaluation of a function describing the relative rates of change of grid lines in the (χ, ζ) and (x, y) coordinate systems. On a uniformly spaced calibration grid, derivatives such as $\frac{\partial \chi}{\partial x}$ can be evaluated by measuring the apparent distances in pixel space between adjacent dots. By organising the polynomial evaluation locations to coincide with the dots in the calibration grid, a least-squares solution for $\boldsymbol{\beta}$ can be found and the Gaussian best-fit transformation thus determined.

2.3. Colour calibration

Images captured by the camera record the attenuation of light intensity from the back-light due to the presence in the tank of red food colouring dye dissolved as a visible proxy for fluid density. For the dye to appear red, green and blue parts of the visible spectrum are preferentially attenuated. Green light is spectrally compact and so should respond close to linearly with respect to changing dye concentration. Furthermore our colour camera has a Bayer array of dichroic colour filters containing twice as many green pixels as red or blue, so it is especially convenient to interrogate the green channel in our video sequences. The colour calibration method used here is informed by the work of Cenedese and Dalziel [24].

A key parameter in our experiments is the tank thickness, so we seek a robust interpretation of observed light intensity in terms of upper and lower bounds on thickness-averaged dye concentration. The Lambert-Beer rule,

$$\frac{\partial I}{\partial s} = -\eta(c) I, \tag{10}$$

describes how light intensity I reduces along a ray path s according to a dye response function $\eta(c)$ that depends on concentration. For passage of a ray through dye of two different concentrations c_1 and c_2 for respective distances s_1 and s_2, we have

$$\begin{aligned} I(s_1 + s_2) &= I(0) e^{-\eta(c_1) s_1} e^{-\eta(c_2) s_2} \\ &= I(0) e^{-(\eta(c_1) s_1 + \eta(c_2) s_2)}. \end{aligned} \tag{11}$$

Provided the dye response is linear, i.e. $\eta(c) = d_1 c + d_2$ for suitable coefficients d_1 and d_2, then the exponent can be expressed in the following form,

$$\eta(c_1) s_1 + \eta(c_2) s_2 = \eta \left(\frac{c_1 s_1 + c_2 s_2}{s_1 + s_2} \right) (s_1 + s_2), \tag{12}$$

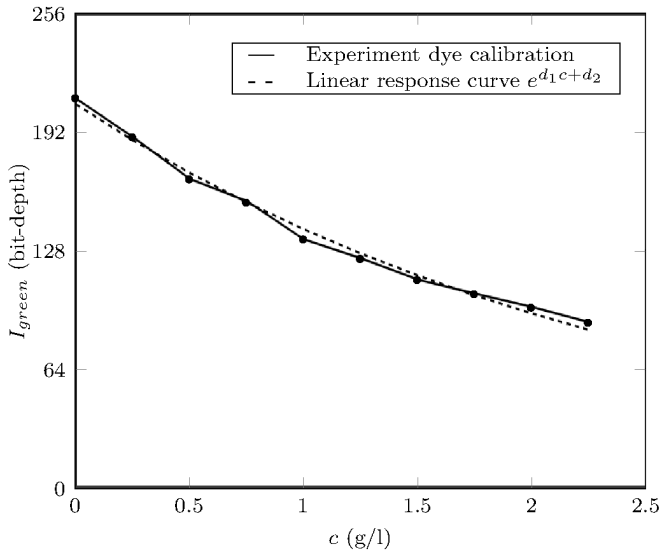

Figure 2: Dye behaviour for 1 mm thick experiments compared to the ideal linear behaviour, where c is dye concentration and I_{green} is the light intensity value on the green channel in the RGB calibration images.

showing that the observed attenuation would measure the along-ray average of the dye concentration. Calibration with several known and uniform concentrations of dye produces the curve shown in figure 2, and for fitted coefficients d_1 and d_2 there is a good linear match at low dye concentrations, though the range over which this is a good approximation decreases with increasing ray path length (and hence with tank thickness). In our thinnest configuration experiments we seek to remain in the dye regime $c < 2g/l$ as dye behaviour is seen to closely follow the linear ideal within this range in figure 2.

With very thin geometries, small changes in experimental setup can have unexpectedly large consequences. The calibrations cover a much broader range of dye concentrations than any experiment, and a minor change in the tank filling procedure for calibration decreased the internal fluid pressure relative to experiment and therefore contracted the tank appreciably. We modify our calibration values to account for the reduced ray-path length by assuming that the attenuation of light in fresh water across the thickness of the tank is negligible, hence the coefficient $d_2 \approx 0$. For an identical uniform dye concentration once an experiment has fully relaxed, the Lambert-Beer relation can be rearranged to give a ratio of tank thicknesses,

$$\frac{s_{\text{exp}}}{s_{\text{cal}}} = \frac{\ln(I_{\text{exp}})}{\ln(I_{\text{cal}})}, \tag{13}$$

that maps colour values from the calibration measurements to equivalents for experiment. We compute bespoke colour mappings for each physical position.

A further complication that arises in experiment is that the acrylic sheeting used for the tank walls deforms under load. The thickness of the tank in its slimmest configuration is of order 1 m, set by the pressure exerted on a pair of rubber O-rings that lie in concentric grooves. Spatial distortion in the tank thickness is significant enough to be measurable, simply by calibrating the ray-path attenuation through a uniformly concentrated dye. The thickness profile we obtain has slight but noticeable hallmarks of the bolt-holes at regular intervals along the sides of the tank (see figure 3), despite the clamping load being distributed through a stiff metal bar. Other features visible in the thickness profile are most likely due to artefacts of the acrylic casting process.

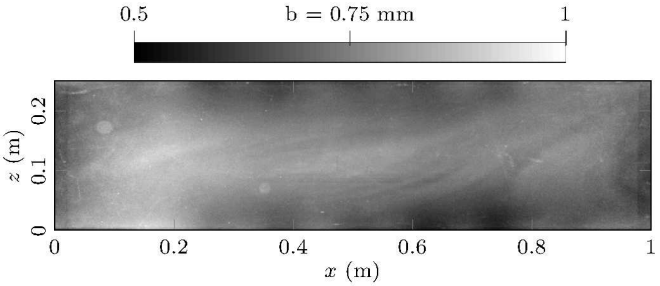

Figure 3: Variation in tank thickness, b, determined by light attenuation through uniform concentration dye.

While it is remarkable to have sufficiently sensitive diagnostics to observe artefacts of manufacturing processes, it clearly indicates that our experiment is operating close to the limit of material tolerances. Since the Ekman parameter λ scales as $\frac{1}{b^2}$, any small thickness variation in the $b = 1$ mm tank configuration may be fluid-mechanically significant and we account for these effects in our numerical simulations by supplying measured point-wise data.

A typical raw camera image $I(\chi, \zeta)$ and corresponding post-processed volume fraction field $\Phi(x, z)$ are shown in figure 4.

3. Initial condition spectra

In this section, we derive an appropriate model for Ekman friction that we will subsequently include in our numerical simulations. We also extend Taylor's linear model to the case with Ekman friction so that we can determine what the $t = 0$ spectral signature must have been from some early-time contours of the experimental scalar field, and show that this closely matches a k^{-1} spectral slope. Later we will use these conditions to initialise our simulations.

3.1. Plane Poiseuille flow

In thin-layer quasi-two-dimensional flows, no-slip boundaries are everywhere proximate and have a profound influence on the evolution of the flow. The appropriate model for the flow between two plates is plane Poiseuille flow. If we restrict the Navier-Stokes to steady incompressible flow in a single direction but account for a velocity profile in the out-of-plane direction, then we have

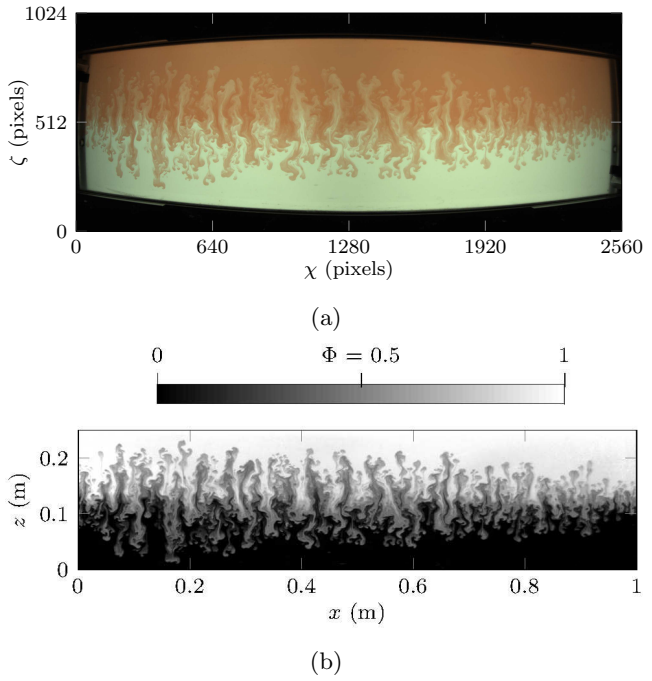

Figure 4: The image processing input and output: (a) the raw experimental image processed to give (b) the volume fraction Φ.

momentum and mass conservation,

$$\begin{aligned} 0 &= -\frac{1}{\rho}\frac{\partial p}{\partial x} + \frac{\mu}{\rho}\frac{\partial^2 u}{\partial y^2} \\ 0 &= \frac{\partial u}{\partial x}, \end{aligned} \tag{14}$$

respectively. Wall friction acts to retard the flow, and so a continuously decreasing pressure in the streamwise direction is needed to maintain velocity and thus satisfy mass and volume conservation in this one-dimensional flow. If the pressure gradient were removed, then the velocity would decay at a rate determined by the wall friction but the problem would be neither incompressible in 1D nor time-invariant. However, by application of equal and opposite forces, we can use the steady case to estimate the instantaneous rate of decay that would occur in the absence of other constraints. We thus treat $\frac{\partial p}{\partial x}$ as a constant and obtain a simple ordinary differential equation,

$$\frac{d^2 u}{dy^2} = -\frac{1}{\mu}\frac{dp}{dx}. \tag{15}$$

Integrating twice in y over the gap between the bounding planes and applying no-slip boundary conditions $u(0) = 0$ and $u(b) = 0$ yields a velocity profile,

$$u(y) = \frac{1}{2\mu}\frac{dp}{dx}(b - y)y. \tag{16}$$

Our goal is to determine the decay rate of in-plane velocity due wall to friction and so in our steady-state model we must compute the pressure gradient $\frac{dp}{dx}$ required to balance this wall force. The total momentum M across the thickness is given by,

$$M = \rho S \overline{u} b = S \int_0^b \rho u(y) dy, \tag{17}$$

where S is a (unit constant) area parameter accounting for the cross-sectional area in the x and z directions. The variable $\overline{u}$ is the mean velocity across the thickness b between the boundaries, the velocity we would aim to compute correctly in analysis or numerical simulation. Substituting for the parabolic velocity profile we have,

$$\begin{aligned} \rho S \overline{u} b &= \frac{S\rho}{2\mu}\frac{dp}{dx}\int_0^b (by - y^2) dy \\ \overline{u} b &= \frac{1}{12\mu}\frac{dp}{dx} b^3, \end{aligned} \tag{18}$$

so we expect the pressure gradient required to maintain velocity $\overline{u}$ to behave as,

$$\frac{dp}{dx} = \left(\frac{12\mu}{b^2}\right)\overline{u}. \tag{19}$$

Conversely, by substitution for the pressure in the one-dimensional momentum equation, we would expect the velocity to decay exponentially according to,

$$\rho\frac{d\overline{u}}{dt} = -\left(\frac{12\mu}{b^2}\right)\overline{u}, \tag{20}$$

and can therefore quantify the *Ekman friction rate*,

$$\lambda = \left(\frac{12\nu}{b^2}\right). \tag{21}$$

Reassuringly, this has the same $\frac{\nu}{b^2}$ scaling as the single walled case in [17] and a larger value of Ekman constant, reflecting the additional curvature of the velocity field due to the additional wall. Although the value we obtain here is around 5 times larger than the comparable value for a semi–infinite domain, it should be stressed that the framing of the problem embeds certain assumptions. In particular our analysis assumes that a linear relationship between stress and strain rate remains valid close to a no–slip boundary in our very thin flows. Motivated by the inconsistencies in the available literature, we sought in this study to confirm our selection of Ekman time–scale by minimising discrepancy in spectral energy between our simulations and experimental data, as discussed in §4.2.

3.2. Taylor's linear growth model

The linear model for Rayleigh-Taylor growth due to Taylor [2] is constructed by considering a sinusoidal perturbation of an interface between a denser upper fluid and a less dense lower fluid. The flow is assumed to be described by velocity potentials,

$$\begin{aligned} \phi_u &= -ae^{-kz+nt}\cos(kx) \\ \phi_l &= ae^{kz+nt}\cos(kx), \end{aligned} \tag{22}$$

for upper and lower layers respectively, with the strength of the potential decaying in the vertical (z) direction away from the interface. The temporal growth rate n is the key unknown. A consistent interfacial profile $\zeta(x)$ is given by a matching condition on the vertical velocity w,

$$w = \frac{\partial \phi}{\partial z} = \frac{\partial \zeta}{\partial t}, \tag{23}$$

and it follows that,

$$\zeta = a\frac{k}{n}e^{nt}\cos(kx), \tag{24}$$

where for small amplitudes we neglect e^{kz} terms in ζ. Taylor integrated the Euler equation for vertical velocity with respect to z to evaluate total pressures in both the upper and lower layers separately, and then employed a matching condition at the interface to close the problem. To account for the influence of Ekman friction on early-stage Rayleigh-Taylor growth, our derivation begins with,

$$\rho\frac{Dw}{Dt} = -\frac{\partial p}{\partial z} + \rho g - \rho\lambda w. \tag{25}$$

We neglect the non-linear transport terms, substitute for velocity potential ϕ and integrate to obtain,

$$\rho\frac{\partial \phi}{\partial t} = -p + \rho g z - \rho\lambda\phi - \overline{p}, \tag{26}$$

where the constant of integration can be interpreted as a gauge pressure $\overline{p}$. The sign convention in upper and lower layers is critical, and we find the following expressions,

$$\begin{aligned} p_u &= \overline{p} - \rho_u g z + \rho_u\dot{\phi}_u + \rho_u\lambda\phi_u \\ p_l &= \overline{p} - \rho_l g z - \rho_l\dot{\phi}_l - \rho_l\lambda\phi_l. \end{aligned} \tag{27}$$

The interfacial pressure balance is given by,

$$\begin{aligned} p_u|_{z=\zeta} &= p_l|_{z=\zeta} \\ \overline{p} - \rho_u g\zeta + \rho_u\dot{\phi}_u + \rho\lambda\phi_u &= \overline{p} - \rho_l g\zeta - \rho_l\dot{\phi}_l - \rho\lambda\phi_l, \end{aligned} \tag{28}$$

and substituting for the velocity potential we have,

$$\begin{aligned} -\rho_u g\zeta + \rho_l g\zeta &= -\rho_u\frac{n^2}{k}\zeta - \rho_l\frac{n^2}{k}\zeta - \rho_u\lambda\frac{n}{k}\zeta - \rho_l\lambda\frac{n}{k}\zeta \\ -g\left(\rho_u - \rho_l\right) &= -\frac{n^2}{k}\left(\rho_u + \rho_l\right) - \frac{n}{k}\left(\rho_u + \rho_l\right)\lambda. \end{aligned} \tag{29}$$

Noting the definition of the Atwood number (6), we obtain a quadratic relationship for the growth exponent,

$$A_t g k = n^2 + \lambda n, \tag{30}$$

which we note in passing reduces to the zero-Ekman case found by Taylor. Only the positive root given by the quadratic formula is consistent with unstable growth. Making the convenient substitution $2\hat{\lambda} = \lambda$ we have,

$$n = -\hat{\lambda} + \sqrt{\hat{\lambda}^2 + A_t g k}. \tag{31}$$

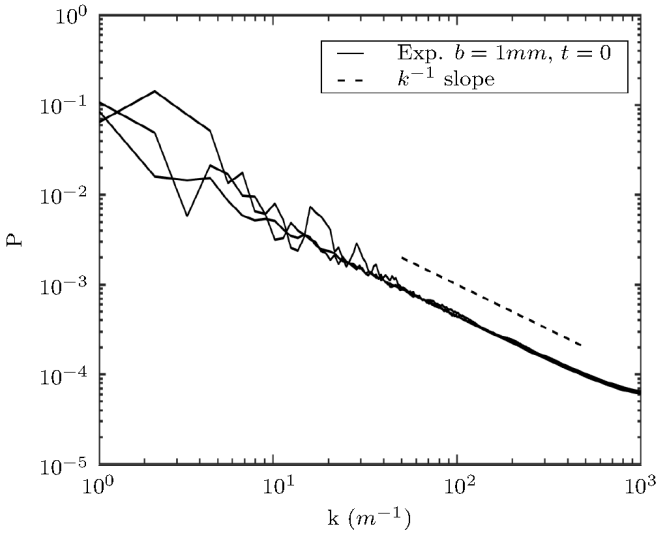

Figure 5: Wind-back of late-linear-regime contour spectra yields experimental initial conditions with a k^{-1} spectrum.

If we consider a circle of radius $\hat{\lambda}$ and a tangent to that circle with length $\sqrt{A_t g k}$, then we may form a right-angled triangle whose hypotenuse exceeds the radius of the circle. The distance by which it exceeds the radius is the remaining growth exponent after Ekman friction is taken into consideration. When Ekman friction is negligible, the circle is small relative to the tangent length and very little growth is lost to friction. With this positive root, for no choice of radius will the tangent ever lie inside the circle so growth, however slow, is always possible.

3.3. Generation of initial conditions

It is well documented that the initial conditions have a significant influence on the growth of Rayleigh-Taylor instability. Close matching of numerical simulation initial conditions with those in the experiments is therefore imperative in order to best match simulation and experiment. The key difficulty lies in measuring experimental conditions at early time, which are not visible at the resolution of a digital camera. Furthermore, experiments are known to become contaminated with low wavenumbers of moderate amplitude at early time, and these have the tendency to dominate later-time behaviour, so it is desirable to capture such effects in simulations that are intended to be an accurate match. As Taylor's linear analysis indicates, eigenmodes of unstable growth directly associate interfacial perturbations with velocity perturbations, however by convention numerical simulations are initialised with only the density field perturbed around the interface and the velocity field is held static. Thus to follow convention we require very low amplitude initial perturbations so that we maximise the inner product of the initial system state and the corresponding unstable eigenmode. Our solution is to take images from experiment at a sufficiently early time that the interface has not yet become multi-valued in each

x ordinate but for which we have a good signal to noise ratio, compute the Fourier transform of a scalar contour $\zeta(x,t)$ and mode by mode 'wind back' time to compute a lower amplitude $\zeta(x,0)$ that is suitable for the initial condition of a numerical simulation.

Given a per-wavenumber estimate of the linear growth rate, we have a simple relationship:

$$\zeta_k(0) = \frac{\zeta_k(t)}{e^{nt}}, \tag{32}$$

utilising the growth rate n derived for Ekman friction influenced Rayleigh–Taylor in (31). Linearity over the spatial spectrum allows us to superpose contributions we obtain from each wavenumber,

$$\zeta(x,0) = \Re\left(\sum_k \zeta_k(0) e^{ikx}\right). \tag{33}$$

The spatial variation in Ekman friction discussed in §3.1 is potentially also significant for the wind-back from observable perturbation of the interface to a suitable initial condition. We therefore take a window-averaged local thickness b to estimate the local temporal growth rate $n(k,b)$, and apply the wind-back locally and to each wavenumber, then compute the superposition over all wavenumbers.

For all quasi-two-dimensional experiments conducted in our study, our inferred initial condition produces a spectral slope of k^{-1}, as indicated in figure 5. Relatively few experimental studies report initial conditions, since these are difficult to obtain directly; Wilson et al. [25] is one of the few that does and they report, using Taylor's hypothesis to convert between temporal and spatial scales, a k^{-5} spectral slope. We note that their mid-plane scalar spectra are measured shortly after flow has left a flat-plate boundary layer, whereas our experimental interface has been accelerated and decelerated rapidly shortly before we measure our early-time contours.

4. Numerical methods

4.1. MOBILE

The calculations described in this article were performed using MOBILE, a parallelized, 3D variable density, finite volume incompressible flow solverhl, and has been validated in detail across a range of mixing flows [11][12][26][27][28]hl, used both to compute direct numerical simulations (DNS) and implicit large eddy simulations (ILES). Mass and momentum are conserved subject to an incompressibility constraint, and a fractional step approach is employed, decoupling hyperbolic (advective transport), parabolic (viscous dissipation and scalar diffusion), and elliptic (pressure/velocity correction) components.

Following ideas of Youngs [29] and Andrews [30] each 1D advection sub-problem is Total Variation Bounded (TVB), both eliminating unphysical oscillations around steep material gradients and maintaining numerical stability for the full 3D problem, even when gradients themselves are not properly resolved. The local Riemann problem across cell faces is solved with Godunov's exact solution, which for this contact discontinuity wave system is trivial, and high spatial order is achieved by modifying the left and right states of the Riemann problem using piecewise polynomial reconstruction of the spatial field. The most obvious linear gradient, m, to choose for a linear reconstruction in the cell located at x_{i-1} has the standard MUSCL form [31],

$$m_{i-1} = \frac{\psi_i - \psi_{i-1}}{2\Delta x}, \tag{34}$$

where ψ represents any of the conserved quantities. A higher order estimate of the gradient can be constructed by using the fluxed volume per unit area $u_{i-\frac{1}{2}}\Delta t$ as a weighting that biases the m_{i-1} gradient as far towards a central difference over the cell face as possible. This more sophisticated gradient has the form,

$$\begin{aligned} m_{i-1} = &\left(1 + \frac{u_{i-\frac{1}{2}}\Delta t}{\Delta x}\right)\frac{\psi_{i-1} - \psi_{i-2}}{3} \\ &+ \left(2 - \frac{u_{i-\frac{1}{2}}\Delta t}{\Delta x}\right)\frac{\psi_i - \psi_{i-1}}{3}, \end{aligned} \tag{35}$$

which is the default choice in MOBILE. Empirical tests have shown that the error scales approximately with $O(\Delta x^n), 2 < n < 3$, even though the stencil retains the spatial compactness of the standard stencil for second order. The order of the method is spatially varying according to local velocity gradients, and a slope limiter of the van-Leer type interpolates the flux between low and high order.

Mutually staggered grids are used for all quantities (velocity and scalar) so there is no co-location of information and maximal coupling for numerical stability. Furthermore, scalar fluxes are computed accurately while requiring only one elliptic pressure solve because scalar quantities are stored at cell centres, while face-normal velocities are stored on their respective faces. Multiple dimensions are decomposed into sequential X-Y-Z-Z-Y-X updates, following the approach of Strang [32] to improve temporal orders of convergence. The projection of this intermediate velocity field onto the nearest vector field in the space of divergence-free fields follows the well-known Hodge-Helmholtz decomposition [33], and exactly conserves discrete angular momentum (a quantity of considerable interest in baroclinic flows), though by construction local conservation of linear momentum cannot be satisfied through the projection. The pressure Poisson equation intrinsic to this projection technique is solved by a highly optimised parallel multigrid algorithm. A parallel macrolanguage interpreter supports convenient on-the-fly computation of turbulent statistics for post-processing and visualization.

For the present simulations of quasi-two-dimensional

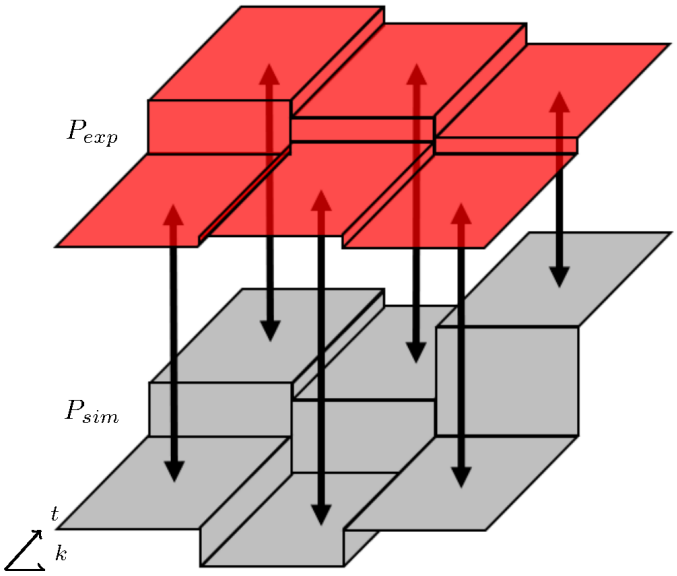

Figure 6: The bin structure in frequency-time space, which is used to calculate mid-plane spectral error between experiment and simulation and in turn to optimise Ekman constant.

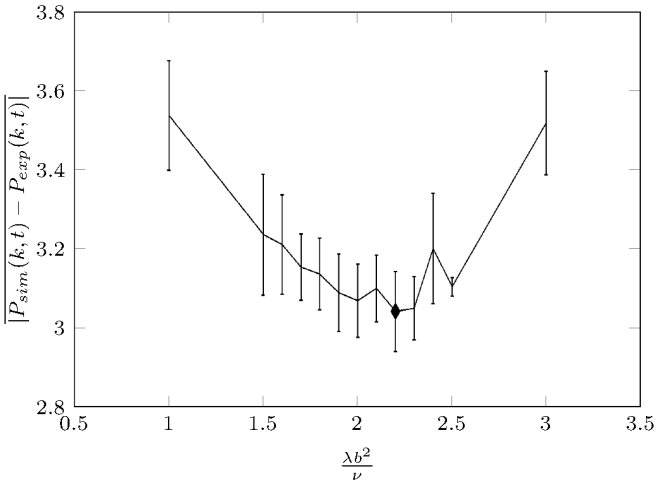

Figure 7: Optimisation of cumulative difference between experiment and simulation mid-plane spectra to give the optimum Ekman constant of 2.2 for the 1 mm thick experiments. Error bars represent the 95% confidence interval, obtained from an ensemble of 10 simulations for each value of Ekman constant.

flow, a scaling analysis of the viscous stresses,

$$\left|\frac{\partial^2 \boldsymbol{u}}{\partial y^2}\right| \gg \left|\frac{\partial^2 \boldsymbol{u}}{\partial x^2} + \frac{\partial^2 \boldsymbol{u}}{\partial z^2}\right| \tag{36}$$

shows that curvatures in the out-of-plane direction far exceed those in the plane, and following the analysis in §3 we account in our numerical models for the dominant source of dissipation. Thus our simulations are a credible approximation to a DNS of the in-plane flow that in this work we term *quasi-DNS*.

4.2. Simulation calibration

With little convergence in the literature on a universal scaling coefficient $\frac{\lambda b^2}{\nu}$ for Ekman friction, proposed values include 0.05 ([16]), $\frac{\pi^2}{4}$ ([34] and [17]), and our analysis of plane Poiseuille flow in §3.1 suggests 12. Rather than trusting our model blindly, we decided to calibrate our (inexpensive 2D) simulations by searching over the Ekman parameter space for a suitable match with experiment.

Digital camera sensors introduce Gaussian random noise, which unavoidably contaminate our experimental measurements. No such difficulties arise for simulation data, but well-known consequences of finitely truncating Taylor's series - as well as more fundamental considerations of strongly non-linear systems - would cause the system state of even the most carefully initialised simulations to diverge over time from a corresponding experimental measurement. Thus we do not seek eddy-for-eddy overlays; instead our focus here is to characterise key statistical quantities from experiment and devise strategies for simulation that can reliably reproduce them, so that other, more accessible, simulation variables can be taken with confidence. Our experiments provide a close proxy for full-field fluid density. Broadly speaking there are two classes of post-processing of the density field that could characterise the instability growth: integral measures of mixing-layer width, and spectral measures of the density field. Spectral statistics are a more challenging target, since they capture aspects of interior morphology that are closely related to instability growth.

We selected the mid-plane transect from the density field because it continuously has a good signal to noise ratio throughout the relaxation lifetime of the instability. By Fourier-transforming to obtain the power spectrum of the density on this transect, and performing the equivalent calculation on the simulations, we can compare whole-lifetime spectra, which may be captured in surfaces $P(k,t)$.

Our penalty function to determine the goodness of fit between experiment and simulation is simply the root-mean-square error between the prediction P_{sim} and measurement P_{exp}, integrated over k and t. Discrete Fourier transforms are widely known to exhibit unwanted artefacts, and a fairer comparison of the spectral surface is found once averaged in wavenumber space and over short periods of time. These reduced-resolution spectral surfaces were compared over a range of simulated values of Ekman parameter, as shown in figure 6.

The results of this calibration are shown in figure 7 and demonstrate sensitivity of our penalty function to variation in the Ekman parameter. The data obtained suggests that for our $b = 1\,\text{mm}$ experiments,

$$\lambda = \frac{2.2\nu}{b^2}, \tag{37}$$

is the appropriate value. The mid-plane spectrum, together with frames of the domain at selected instants in time, is shown in figure 8 for both experiment and the optimal simulation. To further minimise discrepancy be-

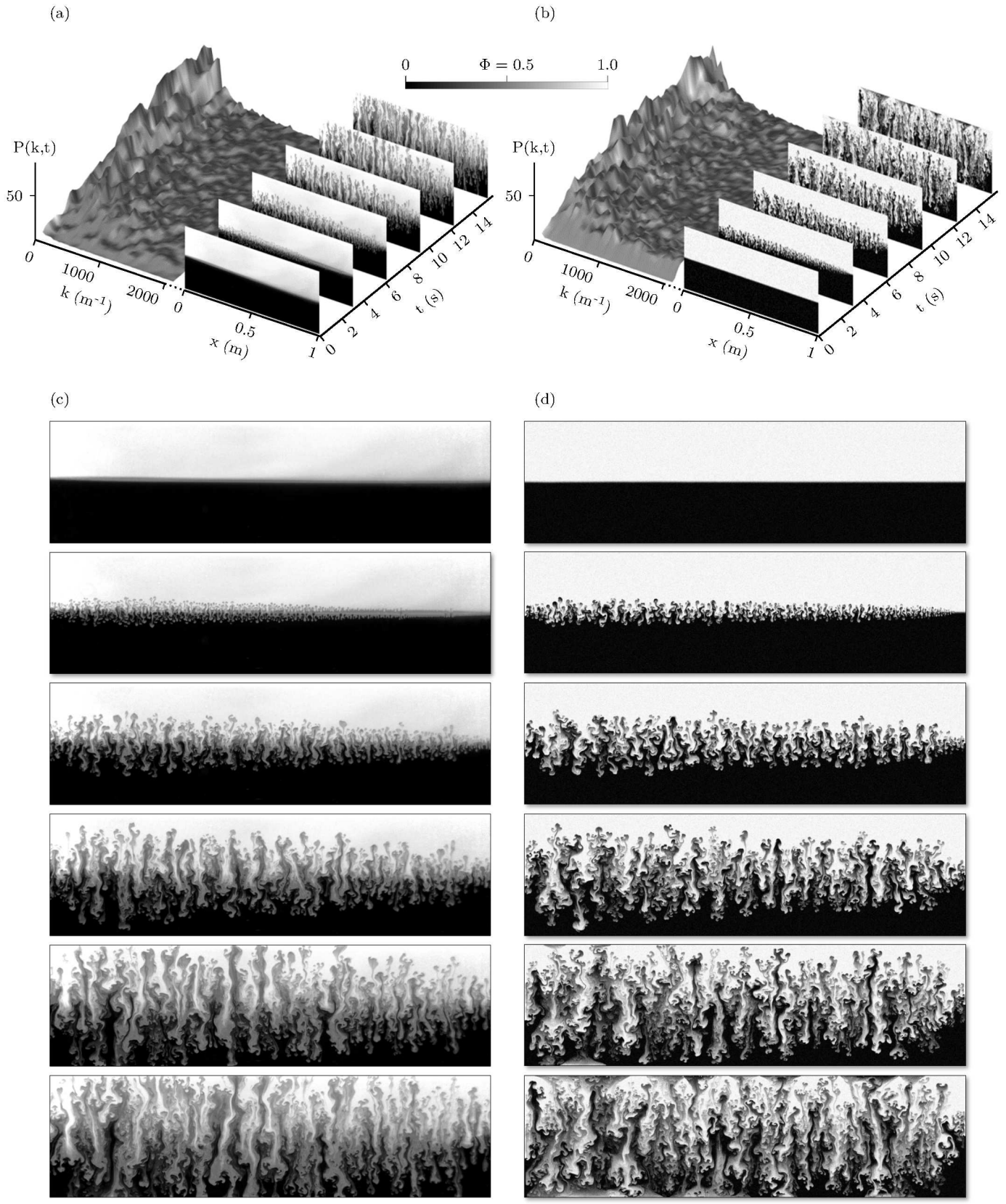

Figure 8: 1D mid-plane volume fraction spectrum development with time for (a) 1 mm thick experiment and (b) corresponding optimised 2D simulation. Volume fraction plots shown again in (c) and (d) respectively for clarity.

tween experiment and simulation, we model the forces on the fluid due to rotation of the experimental apparatus while overturning. The value of Ekman constant given by the optimisation can be considered valid for geometries with similar aspect ratios to ours, in particular those with very small out–of–plane dimension and bounded by two smooth walls. We surmise that in these very thin flows, the assumption of linearity in macroscopic shear stress vs strain rate may be violated near the boundary, so the out–of–plane velocity profile will deviate from predictions of Poiseille.

5. The morphology of Ekman friction

Our measurements from the 1 mm domain have a number of morphological features that bear the hallmarks of Ekman friction. Within this type of experiment there is no way to eliminate Ekman friction, but in simulation we can simply omit the relevant source term to compare the development. A qualitative comparison is shown in figure 9, including insets of enlarged details. We observe very consistently that in these thinnest domains, Ekman friction prevents the classical Rayleigh-Taylor bubble and spike structures from forming in the conventional manner. Instead, as shown in the inset figures, we see *claw-like* structures. We explain these observations by considering how advected material surfaces must respond to Ekman forcing,

$$\frac{d\boldsymbol{u}}{dt} = -\lambda \boldsymbol{u}, \tag{38}$$

imparted by the boundaries. Examining only the vertical component of the velocity, u_z and integrating twice over some short time-scale τ, we obtain the vertical displacement of a material surface,

$$z(\tau) = \frac{u_z(0)}{\lambda}\left(1 - e^{-\lambda\tau}\right) + z(0), \tag{39}$$

which we may characterise by a constant factor $\bar{\lambda}$ as follows: $z(\tau) = u_z(0)\bar{\lambda} + z(0)$. yy a horizontal material surface propagating vertically by passive advection will be exponentially and uniformly retarded and thus retain its shape. However, Rayleigh-Taylor instability is characterised by curved material surfaces penetrating into otherwise quiescent flow. Kinematically the structures are baroclinically induced vortex rings in 3D, and manifest as dipole structures in 2D. In a low-Atwood-number miscible flow these material surfaces emerge from the interior of a rising bubble at the top and are then stretched around the outside surface as they undergo shear against the adjacent descending spike. Thus they travel faster in the absolute reference frame than the bubble itself, and the sides of the bubble travel more slowly. If in the absence of Ekman friction the steady-state propagation of a bubble's dipole or vortex ring at speed u_z is characterised by a persistent velocity differential $u_z + \epsilon$ between its axis and $u_z - \epsilon$ at its fringe, then with Ekman friction the velocity difference will reduce from 2ϵ to $2\bar{\lambda}\epsilon$. This corresponds to a reduction in vorticity, and in the reference frame of the bubble, material surfaces will travel shorter vertical distances and the bubble structure will become progressively squashed into an elliptical shape, The strongest injection of baroclinic vorticity to a bubble is at its fringes where density and pressure gradients are least closely aligned. Provided the bubble has an approximately unit aspect ratio, then it can maintain its structure because along its symmetry plane significant contributions to the induced velocity come from both sides. However the larger the aspect ratio of a bubble, in relative terms the more laterally distant from its centreline become these regions of strong vorticity, until eventually they behave like independent sources of vorticity. The velocity they induce advects the bounding material surface upwards locally to form protrusions, but preserves a relatively shallow gradient near the symmetry plane. Both protrusions are themselves Rayleigh-Taylor-unstable, so form claw-like bifurcations of the bubble and halve the characteristic length-scale. Rayleigh-Taylor instability is understood to develop towards larger length-scales by mode-coupling mechanisms [35], and our geometric constraints limit the down-scale coupling of vorticity and velocity. However, in §6.2 we show that once established, the spectral slopes found in our experiments are remarkably invariant over time, and qualitatively the examples of figures 8 and 9 show tall finger-like structures that persist until late time with little apparent change in the largest lateral length-scales. We anticipate that there may be approximate cancellation of the up-scale and down-scale transfers.

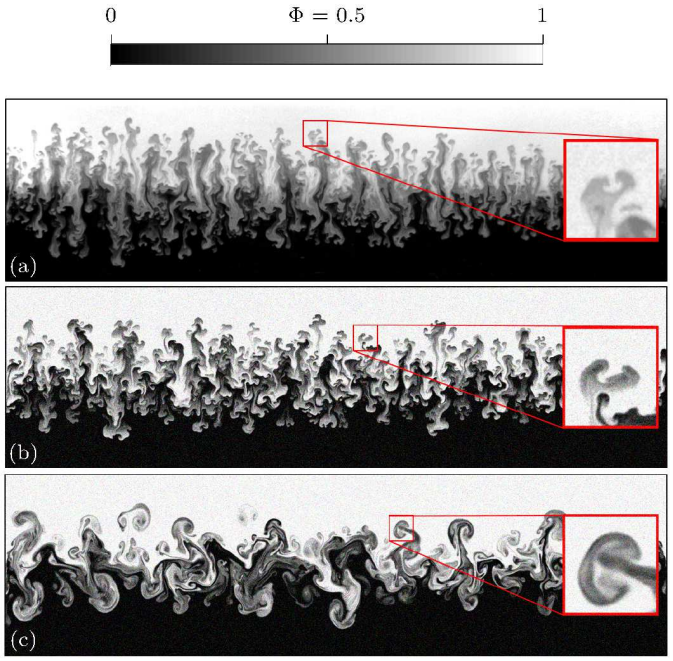

Figure 9: Volume fraction plots showing the structures in the thinnest configuration for (a) 1 mm experiment, (b) 2D simulation with optimised Ekman friction and (c) 2D simulation with no Ekman friction.

6. Domain thickness and instability relaxation

6.1. Probability density functions

The experimental scalar data provides a direct measure of line-of-sight-averaged volume fraction across the domain. The evolution of the volume fraction field from a two-layer unstable stratification to a state that approaches complete mixing is shown in figure 10 for our $b = 1\,\mathrm{mm}$ and $b = 12\,\mathrm{mm}$ experiments, the extremal cases permitted by our experimental approach. Using volume fraction as a suitably accurate proxy for density, we compute its average value for each horizontal z-plane, and plot its evolution over time as a surface $\Phi(z, t)$. Beside this, and in the same orientation on a common t-axis, we provide snapshots of the probability density function (PDF) in the value of volume fraction, once again evaluated for each horizontal z-plane. Especially at early times, the frequency of occurrence of certain values of density is very large, so we show the natural logarithm in the colour scale. The spread of non-zero density values in every z-plane is a measure of the available baroclinic work that can be done to drive further mixing at some time in the future.

At late times it is clear that a broad range of values in the PDF persists for significantly longer in the 1 mm case than in the 12 mm case, indicating that here, considerably more time is required to expend the available energy before the instability relaxes to a well-mixed state. With geometric confinement suppressing down-scale energy transfer, energy remains for longer at larger scales, as shown in figures 8 and 9. By contrast the three-dimensionality accessible to the 12 mm experiment, in particular the mechanism of vertex stretching outlined in §1.2, more rapidly leads to energetic activity at small scales and associated enhancement of molecular-scale mixing, so the range of densities collapses towards the mean over a shorter timescale, and the instability reaches its relaxed state relatively soon. It is quite surprising how sensitive the dynamics appear to be to changes in overall domain aspect ratio.

6.2. Scalar spectra

A Boussinesq fluid, a good approximation for those studied here, has the property of statistical symmetry about the midplane and spectral behaviour at the midplane may be taken as indicative of structure across the whole domain. We compare development of the midplane spectra for experiment and simulation for 1 mm, 6 mm and 12 mm cases in figures 11, 12 and 13. The 1 mm experiment shares the k^{-1} initial spectrum obtained in §3.3 and both the experiment and corresponding simulation maintain a k^{-1} slope throughout. The 6 mm and 12 mm thick test cases see convergence at later time, with the spectral slope in both cases approaching $k^{-\frac{5}{4}}$. The similarity in spectral slope between experiment and simulation at each domain thickness serves to validate the use of MOBILE simulations for modelling these spectral characteristics. However, the differences in the evolution of spectral energy between experiment and simulation at 6 mm and 12 mm thicknesses illustrates the difficulty in matching the two for highly non-self-similar flows.

The spectral surfaces plotted in figure 8 for our 1 mm experiments and discussed in §4.2, indicate a steady accumulation of spectral density at low wavenumbers k over the time-period observed, consistent with the mode selectivity of the Rayleigh-Taylor instability and the up-scale energy transfers prevalent in thin domains when vortex stretching is suppressed. Eventually, all kinetic energy will be dissipated by viscous action, but once bubbles and spikes have reached the vertical extremities of the domain, the characteristic features of developing Rayleigh-Taylor instability cease to be discernible. On the time-scale of our observations, the 6 mm and 12 mm cases shown in figure 14 show an increase in spectral density at low wavenumbers, followed by reduction in low wavenumber components towards the end of our observation period. To characterise this process we consider the development in three phases. The first phase resembles the classic unconstrained three-dimensional Rayleigh-Taylor growth, where the height of the instability is small compared to any of the lateral dimensions. When the growth is of a comparable length scale to the smallest lateral dimension we lose the original form of self-similar behaviour because subsequent growth becomes dependent on a fixed length scale as well as increasing time, so length- and time-scales can no longer increase in proportion. It is evident from the time-slices of domain volume fraction in figure 14 that large structures then develop, consistent with the growth observed in low-wavenumber parts of the spectrum. In order for these structures to form and for their growth to exceed the domain thickness, fluid motions must be primarily in-plane. However, in the third, final, phase, vortex-stretching action becomes sufficiently strong for diffusive processes to rapidly reduce the scalar variance and with it the baroclinic engine that drives further kinematic activity.

6.3. Velocity spectra and growth rate α

Having validated MOBILE simulations for use as a suitable proxy for our experiments, we may now extract data from our simulations that our experimental diagnostic does not make available. We use simulated velocity data to generate energy spectra, shown in figure 15. One striking feature is the similarity between our 6 mm and 12 mm spectra. All spectra have been sampled at a Rayleigh-Taylor development that has reached $h = 20\,\mathrm{mm}$ (though the evolution time at which this arises differs in each case). This strongly suggests that there is a rapid transition away from an Ekman-dominated regime somewhere between 1 mm and 6 mm. Earlier analysis of probability density functions supports the contention that vortex-stretching rapidly becomes active even if geometric confinement continues to constrain the motion beyond the feasible thickness range of our experiments. We observe k^{-3} spectral slopes for energy in the 1 mm case, in–line with expectations from Kraichnan [36] and this persists when out-of-plane degrees

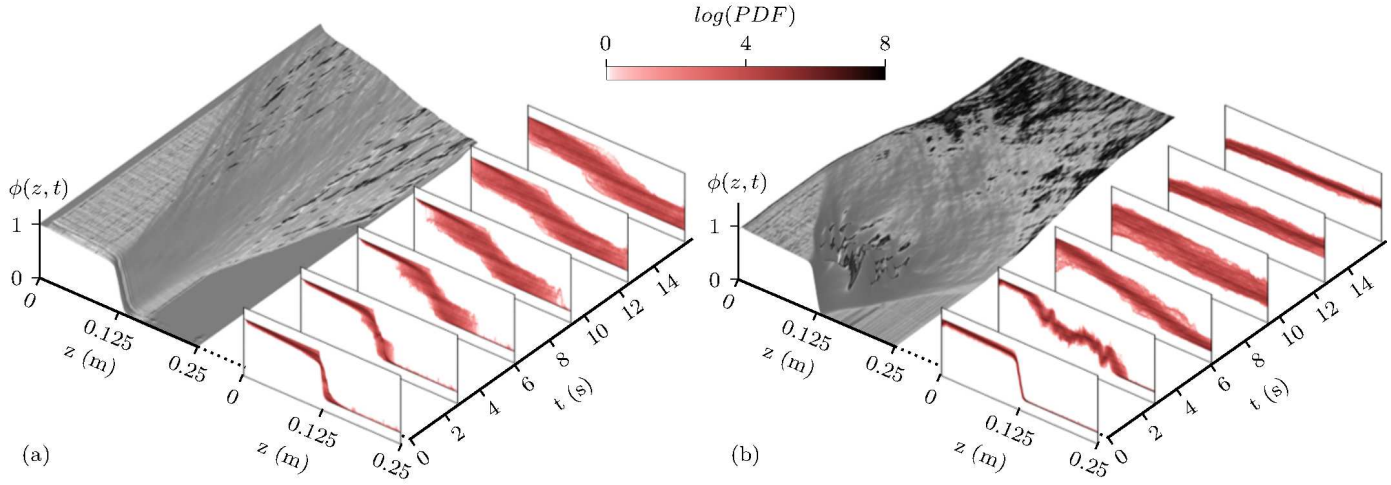

Figure 10: Volume fraction field evolution in time. $\Phi(z,t)$ is plotted as a surface, with volume fraction on the vertical axis, and the probability density function at each z-plane sampled over 100 discrete bins. (a) 1 mm experiment, (b) 12 mm experiment

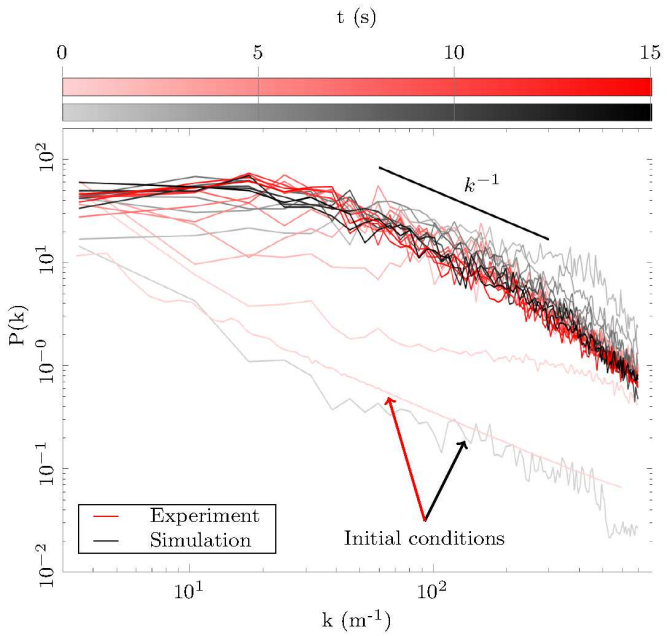

Figure 11: Mid-plane line-of-sight-averaged scalar spectra throughout time for 1 mm thick experiment and 2D simulation, showing close comparison between experiment and simulation.

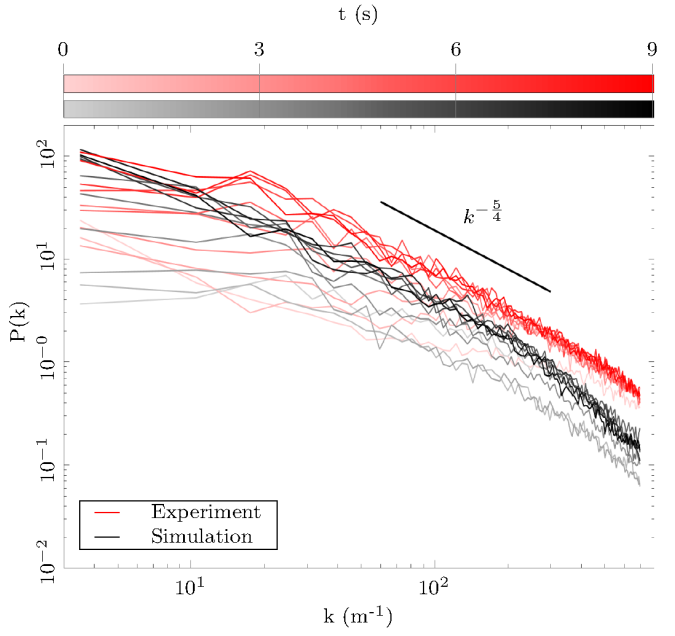

Figure 12: Mid-plane line-of-sight-averaged scalar spectra throughout time for 6 mm thick experiment and simulation. Late time spectral slopes are well matched but differences in the evolution of spectral energy are apparent.

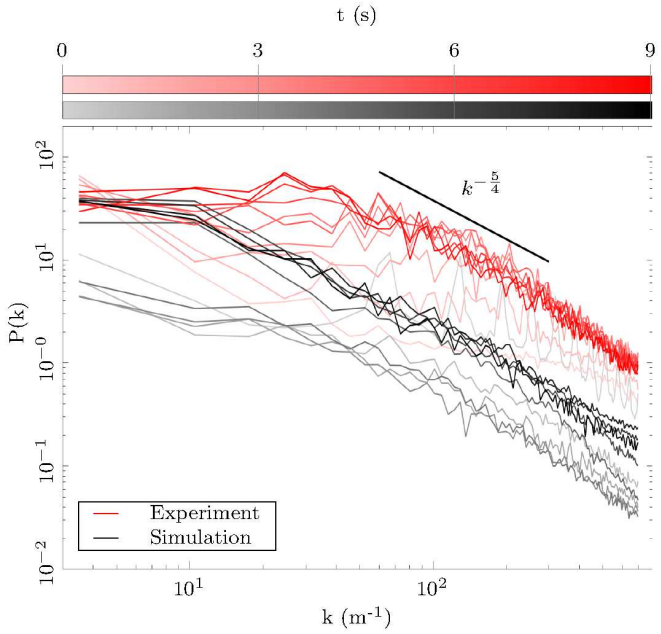

Figure 13: Mid-plane line-of-sight-averaged scalar spectra throughout time for 12 mm thick experiment and simulation. Late time spectral slopes are well matched but differences in the evolution of spectral energy are apparent.

of freedom are introduced to the simulations, so we conclude that this is a property of the geometry. However, it remains unclear why 6 mm and 12 mm cases show steeper rather than shallower slopes reported in [37]. We anticipate that at larger thicknesses than we are able to accommodate, the inertial range slope will revert to $k^{-\frac{5}{3}}$, consistent with previous MOBILE simulations [26] in unconstrained domains.

There is typically a close correspondence between energy and scalar spectra in turbulent flows, but in our 1 mm experiments there has arisen is a very particular set of circumstances. From figure 15 we show that the developed energy spectrum follows an $e(k) = k^{-3}$ scaling. Following the arguments laid out in §1.2, the corresponding enstrophy spectrum is given by $k^2e(k) = k^{-1}$. In figure 5 we demonstrate very clear adherence to a k^{-1} initial scalar spectrum. The crucial connection to make here is that baroclinically generated vorticity must also have an initial spectral scaling of k^{-1}, ensuring that the initial state of the system is perfectly balanced with the geometric constraint that we know from simulation will constrain energy spectra to k^{-3} scaling at later time. Thus, until the bubble and spike structures reach the vertical extrema of the domain, the flow remains in a stable self-similar equilibrium.

It would be reasonable in this special circumstance to expect near-perfect quadratic growth $h(t) = \alpha A_t g t^2$, and in-so-doing provide incontrovertible experimental evidence of self-similarity in the non-linear phase of Rayleigh-Taylor instability. Although on dimensional grounds the scaling cannot be disputed, it has been the work of decades to refine our understanding of the role initial conditions play, and to seek convergence on the scaling parameter α. Since the seminal work of Youngs [6] and Read [7] first posed the question, many experimentalists and computational scientists have sought to claim self-similarity, as summarised by Zhou [38] [39]. The present study, we believe, is the first to convincingly demonstrate it, by a combination of coincidental initial condition and geometric construction. Figure 16 plots an integral measure of mixing-region development, $\hat{h}(t)$, and we note the marked disparity between the self-similar profile for the 1 mm case (with a quadratic curve for comparison fitted at $\alpha = 0.012$) and the non-self-similar adjustments that strongly perturb the growth profiles away from the quadratic ideal for the 6 mm and 12 mm cases. In figure 17 we plot the curves for $b = 1$ mm on a re-scaled time axis to illustrate more clearly that there is no early–stage transient relaxation towards self-similarity. Initial transients routinely arise when the spectral composition of the initial condition is in disequilibrium with the long-term self-similar development. Our experiments are truncated by upper and lower boundaries so we depart from self-similarity at late time as the mixing region approaches the constraints.

We note that the standard integral measure $h(t) = 6\int \overline{\Phi}(1-\overline{\Phi})dz$ [14] recovers a positive value at t=0 for all experimental initial conditions, misleadingly suggesting that significant mixing may have occurred before the experiment begins. A combination of factors are responsible in addition to molecular-scale diffusion of the volume fraction field, amongst them Gaussian camera noise across the entire image and line-of-sight averaging of interface tilt that occurs during initial rotation. By examining 1% and 99% volume fraction contours from fields at $t < 0$ we estimate the contribution to $h(0)$ from interface diffusion to be no greater than 5.4 mm, an order of magnitude smaller than the value computed by this integral measure. Accordingly we present an offset metric $\hat{h} = 6\int \overline{\Phi}(1-\overline{\Phi})dz - \overline{h(0)}$ in figures 16 and 17, with $\overline{h(0)}$ determined from our b=1 mm experiments, and post-process our simulations in a similar manner for direct comparison.

7. Conclusions

We have presented a detailed hybrid experimental-numerical study on Rayleigh-Taylor instability constrained in one lateral dimension to be almost two-dimensional. In our slimmest configuration, the out-of-plane velocity gradients are dominated by Ekman friction against the boundaries and this exponentially drains vorticity from the system. We have discussed the morphological consequences of this action, and highlighted deviation from the conventional models for Rayleigh-Taylor instability. Our experiments were performed over a sequence of domain thicknesses in the most dynamically sensitive range, where two changes occur simultaneously. Firstly Ekman friction reduces inversely with the square of the thickness, and secondly the vorticity vector has more freedom to deviate

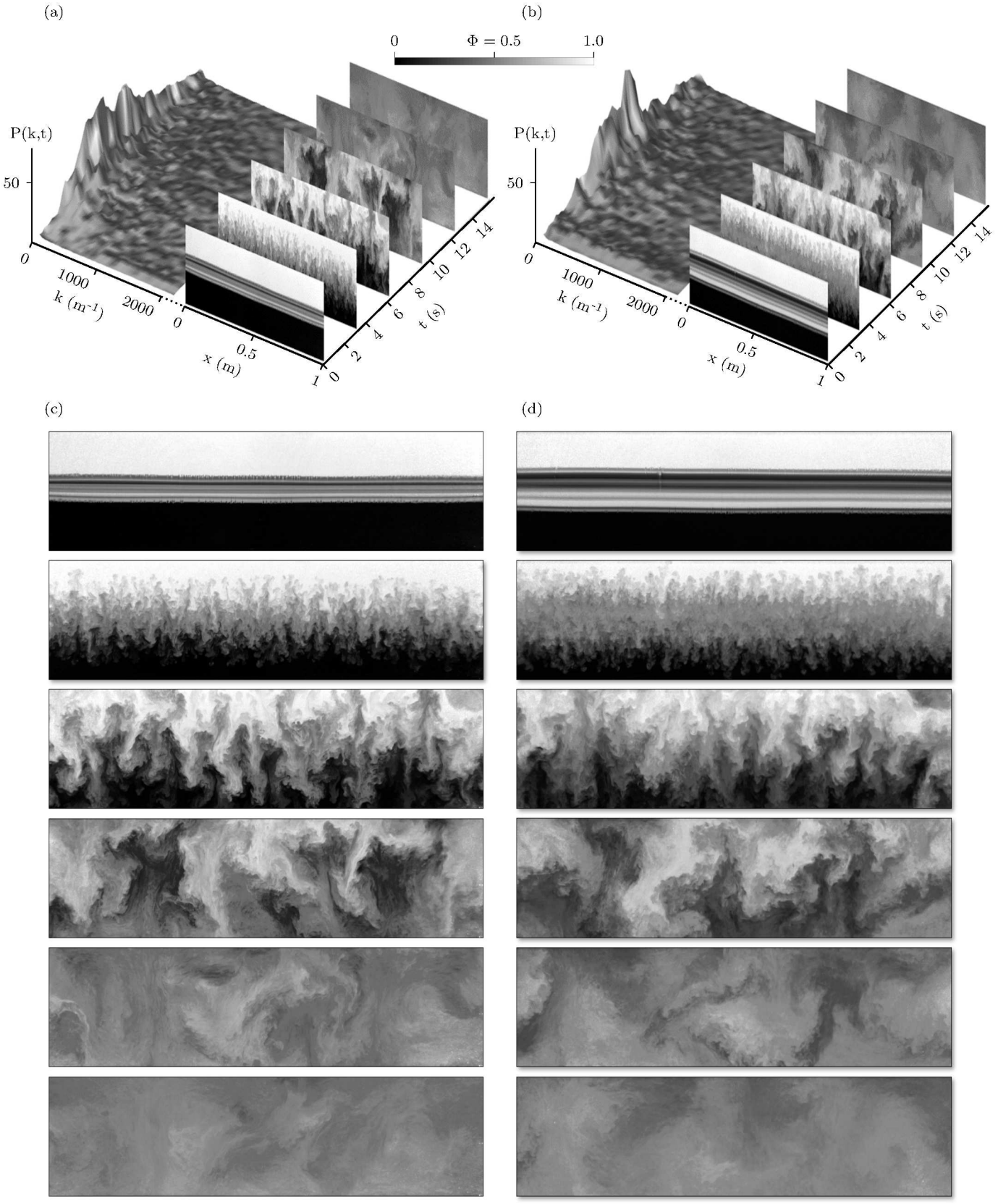

Figure 14: 1D mid-plane volume fraction spectrum development with time for (a) 6 mm thick experiment and (b) 12 mm thick experiment. Volume fraction plots shown again in (c) and (d) respectively for clarity. The horizontal bands at zero time arise due to line-of-sight averaging of shear on the interface during overturning.

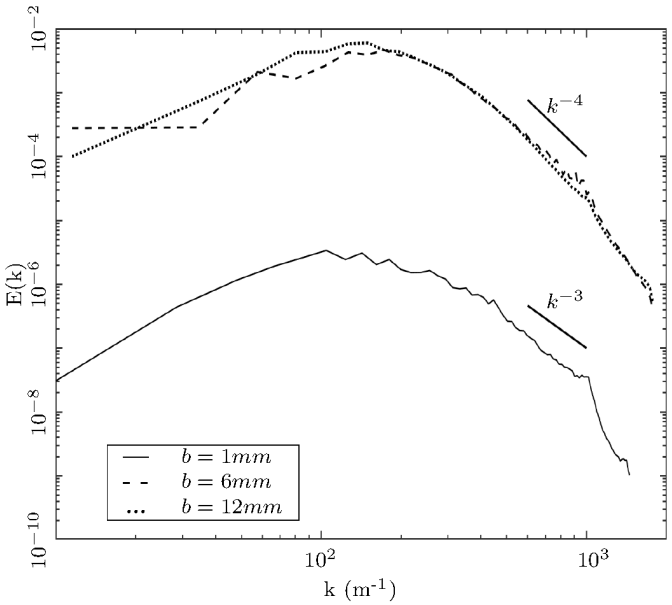

Figure 15: Full velocity field energy spectra for two-dimensional simulation with Ekman friction at 1 mm thickness and three-dimensional simulation at 6 mm and 12 mm thicknesses. Spectra extracted at $h = 20$ mm, corresponding to times where classic Rayleigh-Taylor bubble and spike structures are exhibited.

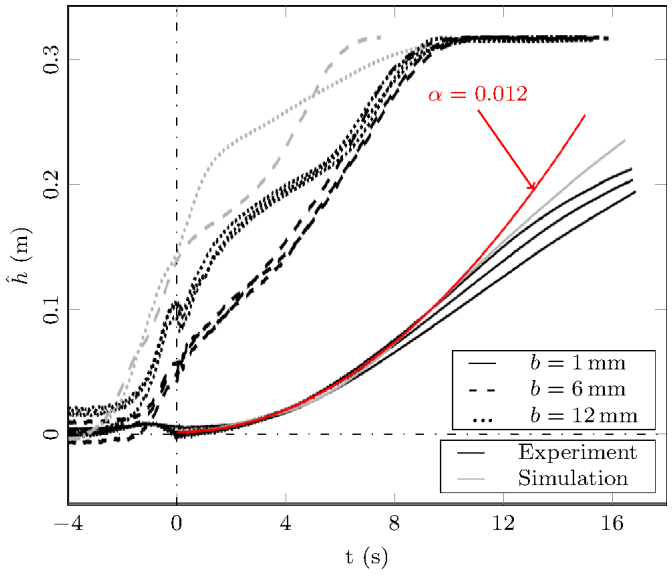

Figure 16: Comparison of mixing region height $\hat{h}(t) = 6\int \overline{\Phi}(1-\overline{\Phi})dz - \overline{h(0)}$ through instability relaxation for a range of domain thicknesses.

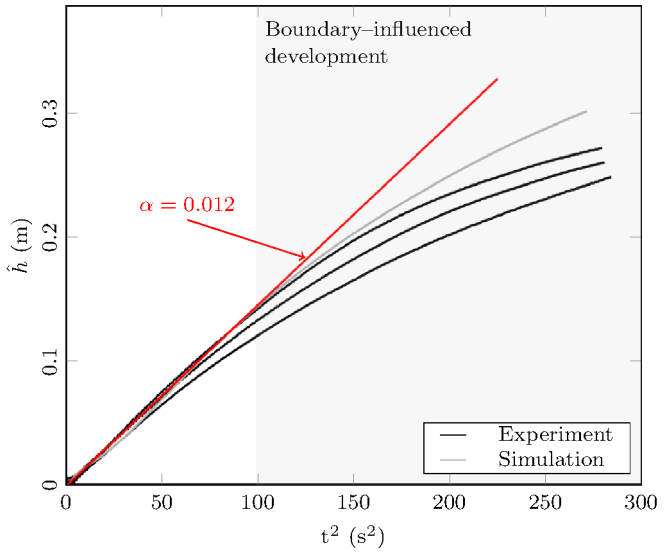

Figure 17: Mixing region height $\hat{h}(t) = 6\int \overline{\Phi}(1-\overline{\Phi})dz - \overline{h(0)}$ through instability relaxation for 1 mm experimental case plotted on a quadratic time axis. True quadratic growth is a straight line on this plot and the experiments match this growth for up to 10 seconds.

from the out-of-plane normal, introducing down-scale cascade dynamics that are not significant in our slimmest configurations. By extending Taylor's linear model of instability growth to account for Ekman friction, we have been able to estimate with some precision the initial condition spectra of our experiments, and find that these very closely follow a k^{-1} spectrum. We then used this spectrum to initialise closely matching simulations, and found an Ekman parameter of $\frac{2.2\nu}{b^2}$ optimally matches mid-plane spectral data through the lifetime of instability relaxation. We were then able to use our MOBILE simulations as a quasi-DNS proxy for our experiments, and extract more detailed statistical and spectral information than is available through our experimental diagnostics. Using this proxy information we have argued that our 1 mm experiments have k^{-3} scaling of energy and therefore k^{-1} scaling of enstrophy, precisely matching the spectral composition of the initial condition. An important and novel consequence of this match is that our configuration eliminates any early-time transient relaxation to the long-term self-similar equilibrium, because it is already aligned with this equilibrium. By expanding the domain from 1 mm to 6 mm and then 12 mm, spanning the feasible range of our experimental approach, we show the structural changes in spectra and instability growth that occur in this most sensitive range, making available to the community a validation resource tightly coupled to an experimental ground-truth.

8. Acknowledgements

We would like to thank AWE for their support and encouragement, and Robin Williams in particular for useful discussions. The funding for this work was under grant:

EPSRC14220081/EP/M507337/1/AWE30331919/0.
This work was carried out using the computational facilities of the Advanced Computing Research Centre, University of Bristol - http://www.bristol.ac.uk/acrc/.

Declarations of interest: none.

References

[1] Lord. Rayleigh, Investigation of the character of the equilibrium of an incompressible heavy fluid of variable density, Scientific papers (1900) 200–207.
[2] G. I. Taylor, The instability of liquid surfaces when accelerated in a direction perpendicular to their planes. i, Proc. R. Soc. Lond. A 201 (1065) (1950) 192–196.
[3] R. Davies, G. I. Taylor, The mechanics of large bubbles rising through extended liquids and through liquids in tubes, Proceedings of the Royal Society of London. Series A. Mathematical and Physical Sciences 200 (1062) (1950) 375–390.
[4] R. Duff, F. Harlow, C. Hirt, Effects of diffusion on interface instability between gases, The Physics of Fluids 5 (4) (1962) 417–425.
[5] D. Layzer, On the instability of superposed fluids in a gravitational field., The astrophysical journal 122 (1955) 1.
[6] D. L. Youngs, Numerical simulation of turbulent mixing by Rayleigh–Taylor instability, Physica D: Nonlinear Phenomena 12 (1-3) (1984) 32–44.
[7] K. Read, Experimental investigation of turbulent mixing by Rayleigh–Taylor instability, Physica D: Nonlinear Phenomena 12 (1-3) (1984) 45–58.
[8] A. G. W. Lawrie, S. B. Dalziel, Rayleigh–Taylor mixing in an otherwise stable stratification, Journal of Fluid Mechanics 688 (2011) 507–527.
[9] M. S. D. Wykes, G. O. Hughes, S. B. Dalziel, On the meaning of mixing efficiency for buoyancy-driven mixing in stratified turbulent flows, Journal of Fluid Mechanics 781 (2015) 261–275.
[10] N. Inogamov, A. Oparin, Bubble motion in inclined pipes, Journal of Experimental and Theoretical Physics 97 (6) (2003) 1168–1185.
[11] A. G. W. Lawrie, S. B. Dalziel, Turbulent diffusion in tall tubes. i. models for Rayleigh–Taylor instability, Physics of Fluids 23 (8) (2011) 085109.
[12] A. G. Lawrie, S. B. Dalziel, Turbulent diffusion in tall tubes. ii. confinement by stratification, Physics of Fluids 23 (8) (2011) 085110.
[13] H. S. Hele-Shaw, The flow of water (1898).
[14] M. J. Andrews, D. B. Spalding, A simple experiment to investigate two-dimensional mixing by Rayleigh–Taylor instability, Physics of Fluids A: Fluid Dynamics 2 (6) (1990) 922–927.
[15] V. W. Ekman, Om jordrotationens inverkan på vindströmmar i hafvet..., Centraltryck, 1902.
[16] G. Boffetta, A. Cenedese, S. Espa, S. Musacchio, Effects of friction on 2d turbulence: An experimental study of the direct cascade, EPL (Europhysics Letters) 71 (4) (2005) 590.
[17] H. Clercx, G. Van Heijst, M. Zoeteweij, Quasi-two-dimensional turbulence in shallow fluid layers: The role of bottom friction and fluid layer depth, Physical review E 67 (6) (2003) 066303.
[18] P. A. Davidson, Turbulence: an introduction for scientists and engineers, Oxford University Press, 2015.
[19] A. Banerjee, M. J. Andrews, 3d simulations to investigate initial condition effects on the growth of Rayleigh-Taylor mixing, I. J. Heat Mass Trans. 52 (17-18) (2009) 3906–3917.
[20] P. Linden, J. Redondo, Molecular mixing in Rayleigh–Taylor instability. part i: global mixing, Physics of Fluids A: Fluid Dynamics 3 (5) (1991) 1269–1277.
[21] S. B. Dalziel, Rayleigh–Taylor instability: experiments with image analysis, Dynamics of Atmospheres and Oceans 20 (1-2) (1993) 127–153.
[22] J. Simpson, P. Linden, Frontogenesis in a fluid with horizontal density gradients, Journal of Fluid Mechanics 202 (1989) 1–16.
[23] M. Ester, H.-P. Kriegel, J. Sander, X. Xu, et al., A density-based algorithm for discovering clusters in large spatial databases with noise., in: Kdd, Vol. 96, 1996, pp. 226–231.
[24] C. Cenedese, S. Dalziel, Concentration and depth fields determined by the light transmitted through a dyed solution, in: Proceedings of the 8th International Symposium on Flow Visualization, Vol. 8, 1998, pp. 1–37.
[25] P. N. Wilson, M. J. Andrews, Spectral measurements of Rayleigh–Taylor mixing at small atwood number, Physics of Fluids 14 (3) (2002) 938–945.
[26] P. Ramaprabhu, V. Karkhanis, A. G. W. Lawrie, The Rayleigh–Taylor instability driven by an accel-decel-accel profile, Physics of Fluids 25 (11) (2013) 115104.
[27] P. Ramaprabhu, V. Karkhanis, R. Banerjee, H. Varshochi, M. Khan, A. Lawrie, Evolution of the single-mode Rayleigh–Taylor instability under the influence of time-dependent accelerations, Physical Review E 93 (1) (2016) 013118.
[28] D. Aslangil, A. Banerjee, A. G. W. Lawrie, Numerical investigation of initial condition effects on Rayleigh–Taylor instability with acceleration reversals, Physical Review E 94 (5) (2016) 053114.
[29] D. L. Youngs, Accurate numerical methods for volume-fraction transport in one-dimensional multifluid flow (1984).
[30] M. Andrews, Accurate computation of convective transport in transient two-phase flow, International journal for numerical methods in fluids 21 (3) (1995) 205–222.
[31] P. Colella, A direct eulerian MUSCL scheme for gas dynamics, SIAM Journal on Scientific and Statistical Computing 6 (1) (1985) 104–117.
[32] G. Strang, On the construction and comparison of difference schemes, SIAM Journal on Numerical Analysis 5 (3) (1968) 506–517.
[33] H. Helmholtz, Über integrale der hydrodynamischen gleichungen, welche den wirbelbewegungen entsprechen (on integrals of the hydrodynamic equations which correspond to vortex motions), Journal für Mathematik Bd. LV. Heft 1 (1858) 4.
[34] M. Satijn, A. Cense, R. Verzicco, H. Clercx, G. Van Heijst, Three-dimensional structure and decay properties of vortices in shallow fluid layers, Physics of fluids 13 (7) (2001) 1932–1945.
[35] A. Rikanati, D. Oron, U. Alon, D. Shvarts, Statistical mechanics merger model for hydrodynamic instabilities, Astroph. J. Suppl. Ser. 127 (2) (2000) 451–457.
[36] R. H. Kraichnan, Inertial ranges in two-dimensional turbulence, The Physics of Fluids 10 (7) (1967) 1417–1423.
[37] W. Cabot, Comparison of two-and three-dimensional simulations of miscible Rayleigh–Taylor instability, Physics of Fluids 18 (4) (2006) 045101.
[38] Y. Zhou, Rayleigh–taylor and richtmyer–meshkov instability induced flow, turbulence, and mixing. i, Physics Reports 720–722 (2017) 1–136.
[39] Y. Zhou, Rayleigh–taylor and richtmyer–meshkov instability induced flow, turbulence, and mixing. ii, Physics Reports 723 (2017) 1–160.